How to cite: *Angew. Chem. Int. Ed.* **2023**, *62*, e202306433
doi.org/10.1002/anie.202306433

All-Solid-State Batteries

The Universal Super Cation-Conductivity in Multiple-cation Mixed Chloride Solid-State Electrolytes

Xiaona Li[+], Yang Xu[+], Changtai Zhao[+], Duojie Wu, Limin Wang, Matthew Zheng, Xu Han, Simeng Zhang, Junyi Yue, Biwei Xiao, Wei Xiao, Ligen Wang, Tao Mei, Meng Gu,* Jianwen Liang,* and Xueliang Sun**

Abstract: As exciting candidates for next-generation energy storage, all-solid-state lithium batteries (ASSLBs) are highly dependent on advanced solid-state electrolytes (SSEs). Here, using cost-effective $LaCl_3$ and $CeCl_3$ lattice (UCl_3-type structure) as the host and further combined with a multiple-cation mixed strategy, we report a series of UCl_3-type SSEs with high room-temperature ionic conductivities over 10^{-3} S cm^{-1} and good compatibility with high-voltage oxide cathodes. The intrinsic large-size hexagonal one-dimensional channels and highly disordered amorphous phase induced by multi-metal cation species are believed to trigger fast multiple ionic conductions of Li^+, Na^+, K^+, Cu^+, and Ag^+. The UCl_3-type SSEs enable a stable prototype ASSLB capable of over 3000 cycles and high reversibility at −30 °C. Further exploration of the brand-new multiple-cation mixed chlorides is likely to lead to the development of advanced halide SSEs suitable for ASSLBs with high energy density.

All-solid-state lithium secondary batteries (ASSLBs) are attractive because of their high safety, high energy density, and application in a wide temperature range.[1] This leads to a highly increased interest in the field of inorganic solid-state electrolytes (SSEs), which are an essential part of ASSLBs. As a prominent representative, sulfide-based SSEs stand out due to their ultra-high room-temperature (RT) ionic conductivities over 10^{-2} S cm^{-1}. However, sulfide SSEs still face serious problems such as narrow electrochemical stability windows and poor interfacial stability toward oxide cathode materials.

Recently, the metal halides Li_aMX_b (M=Y, Sc, In, Zr, etc., X=Cl, Br)[2] have been extensively studied as candidate SSEs in ASSLBs because of their high RT ionic conductivity over 10^{-3} S cm^{-1}, wide electrochemical stability windows, and excellent interfacial stability toward oxide cathode materials. Most of these materials can date back 1980s even though low ionic conductivity was previously obtained.[3] For example, Li_3YCl_6 was reported by Gerd Meyer et al. to show a low ionic conductivity around 10^{-3} S cm^{-1} at 280 °C.[4] Up to date, most reported superionic halide SSEs are mainly based on close-packed anion sublattice, forming monoclinic (Li_3InCl_6,[5] Li_3ScCl_6[6]), orthorhombic ($Li_{2.5}Y_{0.5}Zr_{0.5}Cl_6$,[7] $Li_{2.73}Ho_{1.09}Cl_6$[8]), and trigonal (Li_3ErCl_6,[9] milled-Li_2ZrCl_6[10]) structures. However, these identified halide SSEs are only a small part of ternary halides with monovalent cations (Li^+, Na^+, etc.).[11]

Among numerous crystal structures of ternary halides, UCl_3-type structure is of interest due to its rich channel sites that can both accommodate monovalent cations and provide migration pathways.[12] The UCl_3-type structures (space group $P6_3/m$) can be described as a distorted hexagonal closest packing of spheres that can be generalized to an MX_3 composition (M=La–Gd, X is halogen). The Wyckoff position 6 *h* is occupied by X and M1 atoms occupy the Wyckoff 2*c* position located in the (002) plane

[*] Prof. X. Li,[+] D. Wu, Dr. S. Zhang, Prof. M. Gu, Prof. X. Sun
Eastern Institute for Advanced Study, Eastern Institute of Technology, Ningbo, Zhejiang 315200 (P. R. China)
E-mail: menggu@eias.ac.cn

Y. Xu,[+] Prof. C. Zhao,[+] X. Han, Dr. S. Zhang, J. Yue, Prof. B. Xiao, Prof. J. Liang
Solid State Batteries Research Center, GRINM (Guangdong) Institute for Advanced Materials and Technology, Foshan, Guangdong, 528051 (P. R. China)
E-mail: liangjianwen@grinm.com

M. Zheng, Prof. X. Sun
Department of Mechanical and Materials Engineering, University of Western Ontario, 1151 Richmond St, London, Ontario, N6A 3K7 (Canada)
E-mail: xsun9@uwo.ca

Y. Xu,[+] Prof. T. Mei
School of Materials Science and Engineering, Hubei University, Wuhan 430062 (P. R. China)
E-mail: meitao@hubu.edu.cn

Dr. L. Wang, Dr. W. Xiao, Dr. L. Wang
State Key Laboratory of Nonferrous Metals and Processes, China GRINM Group Co., Ltd., GRIMAT Engineering Institute Co., Ltd., General Research Institute for Nonferrous Metals, Beijing 100088 (China)

[+] These authors contributed equally to this work.

and also form $[MX_9]^{6-}$ polyhedral (Figure 1a). There are six shorter and three longer M–X bonds (Figure 1b), the three X^- in longer bonds are highlighted in Figure 1b. The $[MX_9]^{6-}$ polyhedra can be seen as tricapped trigonal prisms (Figure 1c), with three trigonal prisms capped on each rectangular face (Figure 1d). These $[MX_9]^{6-}$ polyhedra share triangular faces (marked in Figure 1e) to form columns that shift against each other parallel to [001] direction by 1/2*c*. These $[MX_9]^{6-}$ polyhedra also share edges (marked in Figure 1e) to form a hexagonal channel in the [001] direction. The arrangement of the columns provides empty sites (octahedral and trigonal prismatic) in the [001] direction for possible additional cations. Thus, there are a lot of derivatives of the UCl_3-type structure, such as $Na_{0.727}(Na_{0.364}La_{1.637})Cl_6$, $Na_{0.76}(Na_{0.386}Ce_{1.616})Cl_6$.[12] They can be regarded as "solid solutions" at the NaCl-poor side of the NaCl–MCl_3 systems. It has been reported that Na^+ ions usually occupy statistically the (compressed) octahedral sites [001] direction.[12] Some of those derivatives ($Ag(SrSm)Cl_6$, $Na(BaLa)Br_6$, $Na(SrSm)Cl_6$, etc) were identified to be good ionic conductors with an ionic conductivity of around 10^{-4}–10^{-3} S cm^{-1} at 300 °C.[11–13] Recently, our group further developed $SmCl_3$ as a host for halide SSEs that also belong to UCl_3-type derivatives and these $SmCl_3$-based halide SSEs possess high room-temperature (RT) ionic conductivity up to 10^{-3} S cm^{-1}.[14] Yao et al. also reported a $LaCl_3$-based $Li_{0.388}Ta_{0.238}La_{0.475}Cl_3$ with Li^+ conductivity of 3.02×10^{-3} S cm^{-1} at 30 °C.[15] Considering the abundance of UCl_3-type binary trichlorides and their derivatives, there should be lots of possible promising materials with high RT ionic conductivities that have yet to be discovered.

Inspired by the potential fast ion transport and abundant species, here we investigate the synthesis of new multiple-cation mixed chloride SSEs with high ionic conductivity by using the UCl_3-type structure as a host. The influence of different compositions with various metal species on ionic transport properties was also studied. Several cost-effective multiple-cation mixed chloride SSEs with high lithium-ion conductivity over 10^{-3} S cm^{-1} can be fabricated from abundant Al, La, Ce, and Zr with low costs. ASSLBs containing these SSEs and high-Ni $LiNi_{0.88}Co_{0.09}Mn_{0.03}O_2$ (NCM88) cathode demonstrate stable cycling about 3000 cycles at 5 mA cm^{-2}. More importantly, the cation disorder effect leads to universal monovalent transport (Li^+, Na^+, Cu^+, etc.). The respective Cu^+- and Ag^+-loaded materials exhibit high ionic conductivity values of 7.13×10^{-3} and 7.75×10^{-3} S cm^{-1}. The breakthrough of multiple-cation mixed chloride SSEs is ascribed to both the fast monovalent transport via the unique channel structure and the amorphous components.

Different prototype compositions are presented in Figure 2a. Considering the cost, abundance, and structure of the raw materials (Figure S1 and Table S1,2), $LaCl_3$ and $CeCl_3$ were first selected. It was found that after the ball-milling treatment of $LaCl_3$ (or $CeCl_3$, or their mixture) with LiCl, broad peaks assigned to the UCl_3-type structure appeared in the X-ray diffraction (XRD) patterns (Figure 2b and S2). However, the ionic conductivities of these samples (LiCl–$LaCl_3$ (Li–La–Cl), LiCl–$CeCl_3$ (Li–Ce–Cl), LiCl–$(LaCl_3\cdot CeCl_3)_{0.5}$ (Li–LaCe–Cl)) are only about 3–5×10^{-7} S cm^{-1} (Figure 2c and S3). Thus, tetravalent or pentavalent chlorides ($ZrCl_4$, $HfCl_4$, $TaCl_5$) were added to induce further disorder into the structure to improve ionic conductivity. The LiCl–$(LaCl_3\cdot ZrCl_4)_{0.5}$ (Li–LaZr–Cl), LiCl–$(LaCl_3\cdot HfCl_4)_{0.5}$ (Li–LaHf–Cl), LiCl–$(LaCl_3\cdot AlCl_3)_{0.5}$ (Li–LaAl–Cl), and LiCl–$(LaCl_3\cdot TaCl_5)_{0.5}$ (Li–LaTa–Cl) samples still keep the similar XRD patterns (Figure 2b and S4) and possess increased RT ionic conductivities of 3×10^{-4}, 6.7×10^{-5}, 1×10^{-5}, and 1.8×10^{-5} S cm^{-1} (Figure 2c and

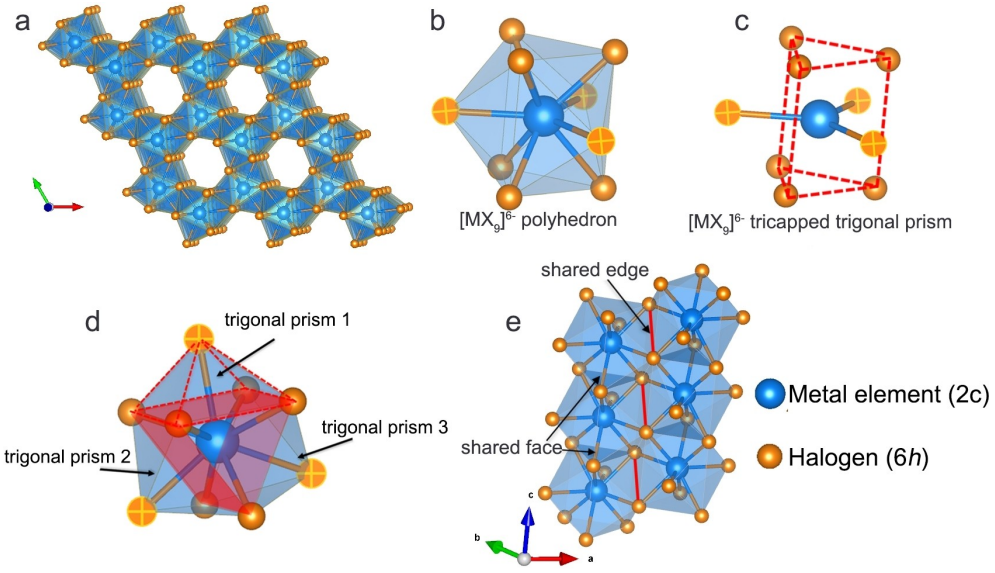

Figure 1. (a) View of UCl_3-type structure along the *c*-axis to show the unit cell with intrinsically existing hexagonal channels. (Metal element, Wyckoff 2*c*, and chlorine, Wyckoff 6 *h*). Illustration of (b) $[MX_9]^{6-}$ polyhedron, (c) $[MX_9]^{6-}$ tricapped trigonal prism with three long bonds and six short bonds, (d) three trigonal prisms in $[MX_9]^{6-}$ polyhedron, and (e) the shared faces and edges of $[MX_9]^{6-}$ polyhedra.

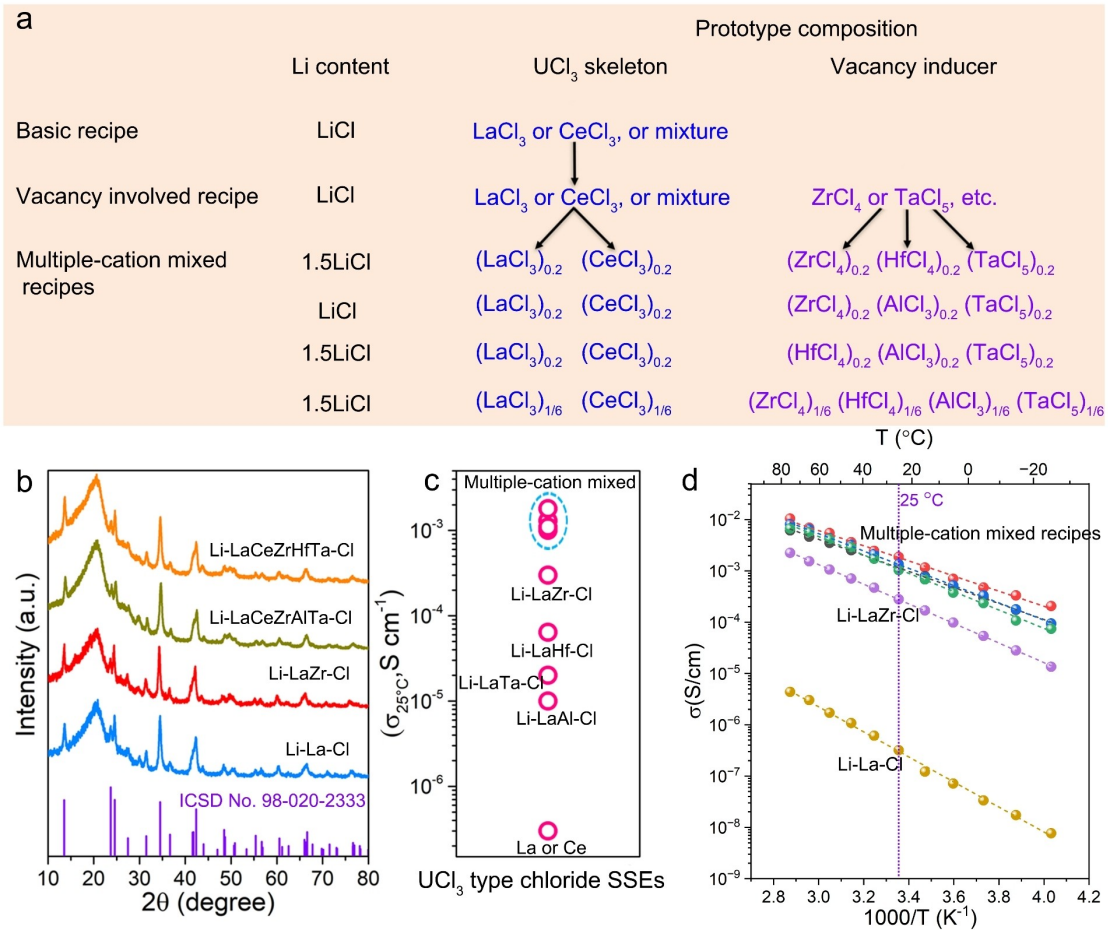

Figure 2. (a) Prototype composition design of UCl_3-type chloride SSEs with different numbers of TM species. (b) XRD patterns of different UCl_3-type chloride SSEs. (c) Ionic conductivities of different UCl_3-type chloride SSEs at 25 °C, and (d) Arrhenius conductivity plots of different UCl_3-type chloride SSEs.

Figure S5). Note that the control samples of 1.5LiCl–$(ZrCl_4 \cdot HfCl_4)_{0.5}$ (Li–ZrHf–Cl) and 1.5LiCl–$TaCl_5$ (Li–Ta–Cl) only show diffraction peaks similar to that of LiCl (Figure S6), demonstrating that $LaCl_3$ or $CeCl_3$ is important to form the final structure and can be regarded as the basic framework of the final materials. The RT ionic conductivities of the control samples are also quite low (Figure S7).

Based on the high ionic conductivity of Li–LaZr–Cl, we then tried to introduce more chlorides (Figure 2a, Table S3) to achieve higher ionic conductivity.[16] Ce^{3+} and Al^{3+} were also selected due to their high abundance and low cost. Higher oxidation states of Nb^{5+} and Ta^{5+} were selected because they are favorable to substitute Zr^{4+}.[17] The results show that further incorporation of $LaCl_3$, $HfCl_4$, $TaCl_5$, $AlCl_3$, or the combination of these chlorides can keep the UCl_3-type structure (Figure 2b and S8), which should benefit from the large configuration entropy of the multiple components. Notably, higher RT ionic conductivities can be achieved for some designed multiple-cation mixed recipes (Figure 2c, Table S3), which include: 1.3×10^{-3} S cm^{-1} for 1.5LiCl–$(LaCl_3 \cdot CeCl_3 \cdot HfCl_4 \cdot AlCl_3 \cdot TaCl_5)_{0.2}$ (Li–LaCeHfAlTa–Cl), 1.8×10^{-3} S cm^{-1} for 1.5LiCl–$(LaCl_3 \cdot CeCl_3 \cdot ZrCl_4 \cdot HfCl_4 \cdot TaCl_5)_{0.2}$ (Li–LaCeZrHfTa–Cl), 1.0×10^{-3} S cm^{-1} for LiCl–$(LaCl_3 \cdot CeCl_3 \cdot ZrCl_4 \cdot AlCl_3 \cdot TaCl_5)_{0.2}$ (Li–LaCeZrAlTa–Cl), and 1.1×10^{-3} S cm^{-1} for 1.5LiCl–$(LaCl_3 \cdot CeCl_3 \cdot ZrCl_4 \cdot HfCl_4 \cdot AlCl_3 \cdot TaCl_5)_{1/6}$ (Li–LaCeZrHfAlTa–Cl). The compositions and ball-milling time have been optimized and RT ionic conductivities of the other contrast samples are also presented in Figure S9 and Table S3. Thus, the RT ionic conductivity can be improved by four magnitudes from the pristine 10^{-7} S cm^{-1} level to the 10^{-3} S cm^{-1} level through the designed multiple-cation mixed strategy (Figure 2c). Figure 2d presents the Arrhenius plots of the ionic conductivities of these multiple-cation mixed chloride SSEs with different metal chlorides. All the obtained activation energy (E_a) values exhibit a lower value of 0.319 to 0.383 eV than that of 0.511 eV of Li–La–Cl SSE (Table S4).

The Raman spectra of the Li–LaCeZrHfTa–Cl and Li–LaCeZrAlTa–Cl SSEs show the finger-print characteristics of the UCl_3-type structures (Figure 3a,b), including the A_g mode assigned to symmetric stretching of Cl elements within *ab* plane (Figure 3c), E_{2g} mode assigned to asymmetric stretching (Figure 3d) and bending of M+Cl elements (M denotes metal cations exclude Li) within ab

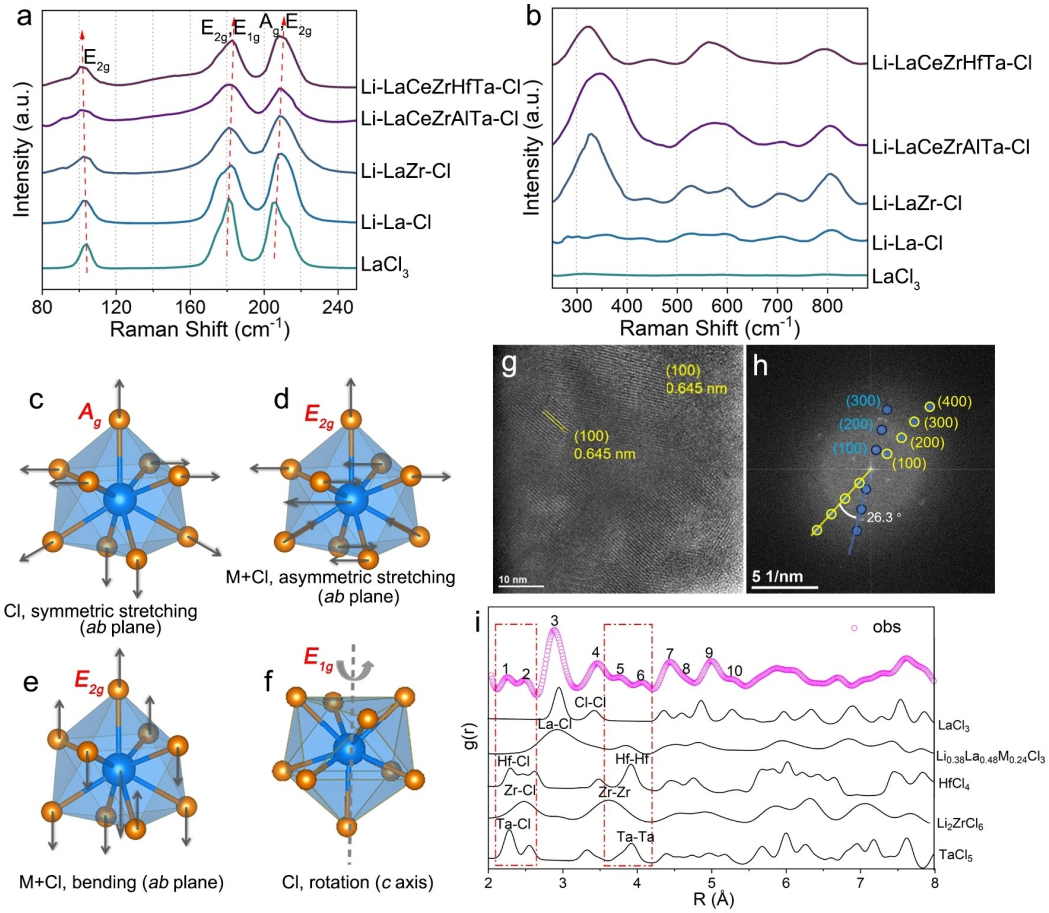

Figure 3. (a,b) Raman spectra of Li–LaCeZrHfTa–Cl, Li–LaCeZrAlTa–Cl, Li–LaZr–Cl, Li–La–Cl, and $LaCl_3$. Raman vibration modes of (c) A_g, (d,e) E_{2g}, and (f) E_{1g} of UCl_3 type structure (C_{6h}^2 point group). (g) HRTEM images taken from the particle edge of Li–LaCeZrHfTa–Cl SSE. (h) The fast Fourier transform (FFT) image of the digitized TEM image, (i) The location region of the PDF results of the Li–LaCeZrHfTa–Cl SSE.

plane (Figure 3e), and E_{1g} mode assigned to rotation about *a*-axis of Cl elements (Figure 3f).[18] The features are different from those of other precursors (Figure S10). The vibrational frequencies seriously in the Li–LaCeZrHfTa–Cl and Li–LaCeZrAlTa–Cl SSEs, demonstrating the elasticity increase of M–Cl bonds caused by the cation disorder within the structure.[19] In addition, the Raman bands in the 300–890 cm^{-1} region display significantly increased intensity and broadened compared with $LaCl_3$ and Li–La–Cl samples (Figure 3f). Considering the fixed geometry and wavelength, the intensity and the Raman bands are highly related to the number of scattering centers, which indicates cation disorder in these samples.[20] The scanning electron microscopy (SEM, Figure S11) and high-resolution transmission electron microscopy (HRTEM) images (Figure 3g,h, S12,13) of the Li–LaCeZrHfTa–Cl SSE indicates that the particle size of the as-synthesized powder is approximately several hundred nm with a large amount of amorphous component (over 50 wt% estimated by a Rietveld refinement method, Figure S14).

The total scattering technique coupled with the Fourier transform (FT) and pair distribution function (PDF) fitting based on the Synchrotron radiation X-ray diffraction and neutron diffraction has been applied to probe the local structure (Figure 3i, S15, Table S5). In addition to the structural peaks of the crystalline phases of the $Li_{0.38}La_{0.48}M_{0.24}Cl_3$ model[15] and $LaCl_3$ (or $CeCl_3$), the PDF results also show many first and second shell peaks of M (M is Ta, Zr, Hf) metal halides such as Li_2ZrCl_6 and $TaCl_5$, etc., demonstrating that local structure of the amorphous part is different from the crystalline phase. The X-ray photoelectron spectroscopy (XPS) high-resolution spectra (Figure S16) show characteristics of Ce^{3+}, La^{3+}, Ta^{5+}, Hf^{4+}, and Zr^{4+} (Table S6), demonstrating that there is no redox reaction during the synthesis. The highly improved ionic conductivities of the multiple-cation mixed chlorides SSEs might benefit from both the intrinsic 1D channels and the possible conduction within the amorphous contents or the interfaces.

Inspired by the structural information of those multiple-cation mixed chlorides, the large-sized UCl_3-type skeleton, and the latest works about $SmCl_3$-based[14] and $Li_{0.388}Ta_{0.238}La_{0.475}Cl_3$[15] SSEs, it is assumed that the UCl_3-type skeleton can intake various materials into the skeleton. We verified this concept by replacing LiCl with

Li_2O and further evaluated the possible conduction behavior for other monovalent cations with small radii, including Na^+, K^+, Cu^+, and Ag^+ (radius in Table S7). These samples were synthesized by the same procedure by replacing LiCl with corresponding chemicals for the optimized Li–LaCeZrHfTa–Cl recipe (Table S3). Thus, the samples were denoted as Li–LaCeZrHfTa–OCl, Na–LaCeZrHfTa–Cl, K–LaCeZrHfTa–Cl, Cu–LaCeZrHfTa–Cl, and Ag–LaCeZrHfTa–Cl, respectively. The XRD patterns of these samples in Figure 4a, S17 still predominantly keep the UCl_3-type structure with weak peaks caused by impurities (marked asterisks), further demonstrating the ability of the UCl_3 structure to accommodate different chemicals. The basic Raman characteristics remain the same for all the samples except for the K–LaCeZrHfTa–Cl sample (Figure 4b), which can be attributed to the large size of K^+. It is supposed that smaller-sized cations should possess better migration ability within the UCl_3 skeleton.

The Li–LaCeZrHfTa–OCl sample possesses similar RT ionic conductivity around 10^{-3} S cm^{-1} compared to its chloride counterpart (Figure S18). To our surprise, as presented in Figure 4c–f, the Cu–LaCeZrHfTa–Cl and Ag–LaCeZrHfTa–Cl (Figure S19) exhibit a very high RT Cu^+ and Ag^+ conductivity of 7.13×10^{-3} S cm^{-1} and 7.75×10^{-3} S cm^{-1}, respectively. The Na–LaCeZrHfTa–Cl sample shows a moderate Na^+ conductivity of 0.88×10^{-3} S cm^{-1} at 25 °C. In contrast, the K–LaCeZrHfTa–Cl sample shows a low K^+ conductivity of 1.32×10^{-6} S cm^{-1} even at 55 °C. The K–LaCeZrHfTa–Cl sample also exhibits a large E_a value of 0.552 eV compared to that of 0.264–0.283 eV of Cu–LaCeZrHfTa–Cl and Ag–LaCeZrHfTa–Cl samples (Figure 4g, Table S8). As we proposed before, the UCl_3 skeleton functioned as a zeolite that can accommo-

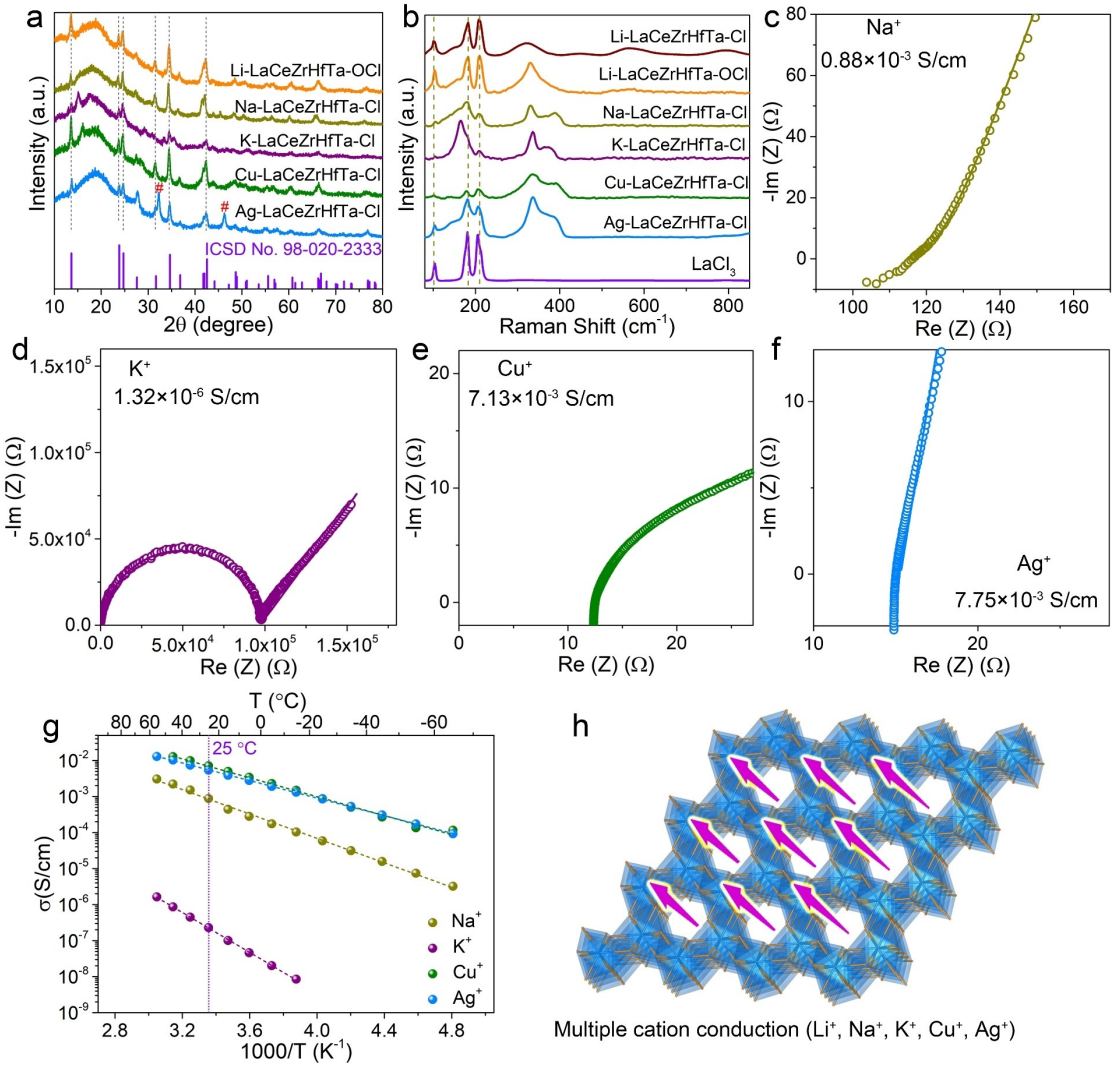

Figure 4. (a,b) XRD patterns of Li–LaCeZrHfTa–OCl, Na–LaCeZrHfTa–Cl, K–LaCeZrHfTa–Cl, Cu–LaCeZrHfTa–Cl, and Ag–LaCeZrHfTa–Cl samples. Nyquist plots for (c) Na–LaCeZrHfTa–Cl (25 °C), (d) K–LaCeZrHfTa–Cl (55 °C), (e) Cu–LaCeZrHfTa–Cl (25 °C), and (f) Ag–LaCeZrHfTa–Cl (25 °C). (g) Arrhenius conductivity plots of different UCl_3-type chloride SSEs. (h) Schematic illustration of universal multiple cation conduction of the UCl_3-type SSEs.

date different chemicals by the mechanical ball-milling method.[14] Although the different obtained conductivities, it is demonstrated that these mobile ions should possess similar diffusion paths and migration mechanisms (Figure S20). To the best of our knowledge, this is the first report of universal monovalent cation conductions in chloride-based materials (Figure 4h), which is different from the metal–organic framework materials..[21]

Among the presented several multiple-cation mixed chloride SSEs, Li–LaCeZrHfTa–Cl SSE was selected to evaluate its application in ASSLBs due to its high RT ionic conductivity. Commercial uncoated single-crystal $LiNi_{0.88}Co_{0.09}Mn_{0.03}O_2$ (NCM88, morphology shown in Figure S21,22) was used as active cathode material to characterize the intrinsic oxide cathode/Li–LaCeZrHfTa–Cl compatibility. The cathode composite (morphology shown in Figure S23) was prepared by mixing NCM88, Li–LaCeZrHfTa–Cl, and acetylene black in a weight ratio of 70:30:1. InLi was used as the anode electrode. The ASSLBs show a discharge and charge capacity of 217.2 and 244.8 mAh g^{-1} (based on NCM88) at 0.125 mA cm^{-2} (0.1 C) at 25 °C, corresponding to an initial Coulombic efficiency of 88.7 % (Figure 5a). The charge/discharge curves show clearly redox plateaus between 2.5 and 4.3 V (vs. Li$^+$/Li), which are similar to those reported NCM88 cells using liquid electrolytes.[22] Figure 5a, S24 also shows the excellent rate capability of the NCM88 ASSLBs, with a reversible capacity of 92 mAh g^{-1} achieved at 6.25 mA cm^{-2} (5 C). The Li$^+$ diffusion coefficient was calculated from galvanostatic intermittent titration test (GITT) curves as referred to in the previous reports.[23] During both the charge and discharge processes, the SSE layer resistance (R_{SSE}) and SSE/cathode interfacial resistance ($R_{SSE\text{-}cathode}$) almost did not change (Figure 5b,c, Figure S25). The evolution of $D_{Li+}S^2V_m^{-2}$ value during the charge/discharge process should be mainly caused by the structural transition of NCM88 due to the proven good interfacial stability within the cathode composites and the stability of the Li–LaCeZrHfTa–Cl SSE in the working voltage range (Figure S26).

The long-term cycling stability of the NCM88 ASSLBs was evaluated at various current densities. The NCM88 ASSLBs can stable cycling for 3000 cycles with a high capacity-retention of 80 % at high current densities of 5 mA cm^{-2} (4 C) (Figure 5d), which should benefit from the compatible and stable cathode/electrolyte interface that guarantees fast charge transfer during charge/discharge process. The performance is comparable to that of ASSLBs

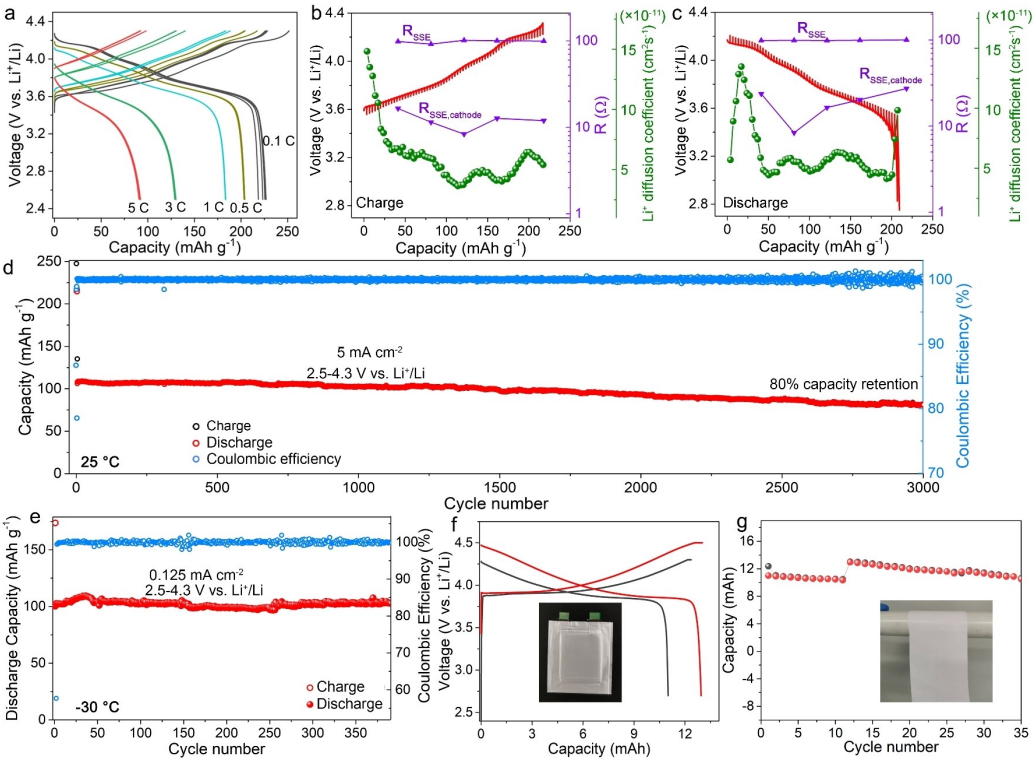

Figure 5. (a) Charge/discharge curves of NCM88 ASSLBs at various current densities (cut-off voltage: 2.5–4.3 V vs. Li$^+$/Li) at 25 °C. GITT profiles (constant current charge in 0.125 mA cm^{-2} for 10 mins and OCV rest for 2 hours) during (b) charge and (c) discharge states. The evolution of resistance of the solid-state electrolyte layer (R_{SSE}) and interfacial resistance between the solid-state electrolyte and cathode ($R_{SSE,\ cathode}$) was also presented. (d) Long-term cycling performance of the NCM88 ASSLBs at 4 C (5 mA cm^{-2}, 2.5–4.3 V vs. Li$^+$/Li) at 25 °C. (e) Cycling performance of the NCM88 ASSLB at 0.1 C at −30 °C. (f) Charge/discharge curves of all-solid-state $LiCoO_2$ pouch cells and (g) the cycling stability at room temperature at 0.03 C (2.7–4.3 V and 2.7–4.5 V vs. Li$^+$/Li) at 25 °C (typical Li–LaCeZrHfTa–Cl SSE sheet fabricated by a solvent-free process). Cathode composite: NCM88 and Li–LaCeZrHfTa–Cl with a weight ratio of 7:3, solid electrolyte bi-layer: Li–LaCeZrHfTa–Cl (contact with cathode) and commercial Li_6PS_5Cl (contact with anode), anode: In–Li foil.

based on halide SSEs that reported recently (Table S9). Additional battery cycling testing can be found in Figure S27,28. The NCM88 ASSLBs also exhibit excellent cycling stability at a low temperature of −30 °C, with a reversible capacity of 102 mAh g^{-1} remaining at 0.125 mA cm^{-2} after 390 cycles (Figure 5e). This extraordinary battery performance at both RT and a low temperature of −30 °C indicates the new Li–LaCeZrHfTa–Cl SSE is a highly promising candidate for high-performance ASSLBs, particularly for low-temperature applications. More importantly, all-solid-state pouch cells with commercial $LiCoO_2$ cathode and bilayer Li–LaCeZrHfTa–Cl and Li_6PS_5Cl SSE membranes deliver a high capacity of 11 mAh at 0.03 C and an initial Coulombic efficiency of 90.7 % when cycled at 2.5–4.3 V vs. Li^+/Li (Figure 5f, g). Higher reversible capacity can be obtained when further increasing the upper voltage to 4.5 V vs. Li^+/Li and a stable cycling can still be achieved, demonstrating the high oxidation stability of the Li–LaCeZrHfTa–Cl SSE.

In summary, a series of superionic chloride SSEs were designed by a multiple-cation mixed strategy and synthesized by a mechanochemical technique. The RT Li^+ conductivities of these multiple-cation mixed chloride SSEs can be significantly improved by four orders of magnitude compared to common LiCl–$LaCl_3$ (UCl_3 type) SSE. The increasing elasticity of the M–Cl bonds is verified, indicating the cation disorder within the multiple-cation mixed chloride SSEs. In addition to the fast ion migration via the UCl_3-type host structure, the ion migration within the amorphous component can not be ignored. These multiple-cation mixed chloride SSEs also possess good compatibility with oxide cathode materials and wide electrochemical windows, affording ASSLBs that cycle stably at RT (3000 cycles) and −30 °C (390 cycles). Our work highlights that creating more configurational disorder within cation sites is an important strategy for promoting fast Li^+ migration. More importantly, these multiple-cation mixed chloride SSEs are one of the first promising classes of frameworks for multiple cation conductions (Li^+, Na^+, Cu^+, Ag^+) over 10^{-3} S cm^{-1}. Our study further enriches the family of UCl_3-type SSEs, and expect that our study will assist in identifying new directions for SSEs for high-performance batteries.

Acknowledgements

This research was supported by the National Natural Science Foundation of China (No. 22379127, 52176185), the Guangdong High-level Innovation Institute project (2021B0909050001), Natural Sciences and Engineering Research Council of Canada (NSERC), Canada Research Chair Program (CRC), Canada Foundation for Innovation (CFI), Ontario Research Fund, University of Western Ontario, and Eastern Institute of Technology, Ningbo.

Conflict of Interest

The authors declare no conflict of interest.

Data Availability Statement

The data that support the findings of this study are available from the corresponding author upon reasonable request.

Keywords: All-Solid-State Battery · Halide Solid Electrolyte · Multiple Cation · Solid-State Electrolyte · UCl_3 Structure

[1] a) D. H. Tan, Y.-T. Chen, H. Yang, W. Bao, B. Sreenarayanan, J.-M. Doux, W. Li, B. Lu, S.-Y. Ham, B. Sayahpour, *Science* **2021**, *373*, 1494–1499; b) L. Ye, X. Li, *Nature* **2021**, *593*, 218–222.
[2] a) T. Asano, A. Sakai, S. Ouchi, M. Sakaida, A. Miyazaki, S. Hasegawa, *Adv. Mater.* **2018**, *30*, 1803075; b) Y. Nikodimos, W. N. Su, B. J. Hwang, *Adv. Energy Mater.* **2023**, *13*, 2202854.
[3] a) W. Weppner, R. Huggins, *Phys. Lett. A* **1976**, *58*, 245–248; b) H.-J. Steiner, H. D. Lutz, *Z. Anorg. Allg. Chem.* **1992**, *613*, 26–30.
[4] A. Bohnsack, F. Stenzel, A. Zajonc, G. Balzer, M. S. Wickleder, G. Meyer, *Z. Anorg. Allg. Chem.* **1997**, *623*, 1067–1073.
[5] X. Li, J. Liang, N. Chen, J. Luo, K. R. Adair, C. Wang, M. N. Banis, T. K. Sham, L. Zhang, S. Zhao, *Angew. Chem. Int. Ed.* **2019**, *58*, 16427–16432.
[6] J. Liang, X. Li, S. Wang, K. R. Adair, W. Li, Y. Zhao, C. Wang, Y. Hu, L. Zhang, S. Zhao, *J. Am. Chem. Soc.* **2020**, *142*, 7012–7022.
[7] K.-H. Park, K. Kaup, A. Assoud, Q. Zhang, X. Wu, L. F. Nazar, *ACS Energy Lett.* **2020**, *5*, 533–539.
[8] J. Liang, E. van der Maas, J. Luo, X. Li, N. Chen, K. R. Adair, W. Li, J. Li, Y. Hu, J. Liu, *Adv. Energy Mater.* **2022**, *12*, 2103921.
[9] R. Schlem, S. Muy, N. Prinz, A. Banik, Y. Shao-Horn, M. Zobel, W. G. Zeier, *Adv. Energy Mater.* **2020**, *10*, 1903719.
[10] K. Wang, Q. Ren, Z. Gu, C. Duan, J. Wang, F. Zhu, Y. Fu, J. Hao, J. Zhu, L. He, *Nat. Commun.* **2021**, *12*, 4410.
[11] G. Meyer, M. S. Wickleder, *Simple and complex halides*, *Handbook on the Physics and Chemistry of Rare Earths*, *Vol. 28*, Elsevier, Amsterdam, **2000**, pp, 53–129.
[12] G. Meyer, S. Masselmann, *Chem. Mater.* **1998**, *10*, 2994–3004.
[13] M. S. Wickleder, G. Meyer, *Z. Anorg. Allg. Chem.* **1998**, *624*, 1577–1582.
[14] J. Fu, S. Wang, J. Liang, S. H. Alahakoon, D. Wu, J. Luo, H. Duan, S. Zhang, F. Zhao, W. Li, *J. Am. Chem. Soc.* **2023**, *145*, 2183–2194.
[15] Y.-C. Yin, J.-T. Yang, J.-D. Luo, G.-X. Lu, Z. Huang, J.-P. Wang, P. Li, F. Li, Y.-C. Wu, T. Tian, Y.-F. Meng, H.-S. Mo, Y.-H. Song, J.-N. Yang, L.-Z. Feng, T. Ma, W. Wen, K. Gong, L.-J. Wang, H.-X. Ju, Y. Xiao, Z. Li, X. Tao, H.-B. Yao, *Nature* **2023**, *616*, 77–83.
[16] Y. Zeng, B. Ouyang, J. Liu, Y.-W. Byeon, Z. Cai, L. J. Miara, Y. Wang, G. Ceder, *Science* **2022**, *378*, 1320–1324.
[17] S.-K. Jung, H. Gwon, H. Kim, G. Yoon, D. Shin, J. Hong, C. Jung, J.-S. Kim, *Nat. Commun.* **2022**, *13*, 7638.
[18] a) J. Murphy, H. Caspers, R. Buchanan, *J. Chem. Phys.* **1964**, *40*, 743–753; b) N. Satyavathi, N. Rajeswar Rao, *Pramana* **1979**, *12*, 139–150.
[19] I. Zakir'yanova, A. Salyulev, *Russ. Metall.* **2010**, 112–115.

[20] a) H. Cynn, O. L. Anderson, M. Nicol, *Pure Appl. Geophys.* **1993**, *141*, 415–444; b) P. McMillan, M. Akaogi, E. Ohtani, Q. Williams, R. Nieman, R. Sato, *Phys. Chem. Miner.* **1989**, *16*, 428–435.
[21] a) S. S. Park, Y. Tulchinsky, M. Dincă, *J. Am. Chem. Soc.* **2017**, *139*, 13260–13263; b) E. M. Miner, S. S. Park, M. Dincă, *J. Am. Chem. Soc.* **2019**, *141*, 4422–4427.
[22] a) X. Fan, X. Ou, W. Zhao, Y. Liu, B. Zhang, J. Zhang, L. Zou, L. Seidl, Y. Li, G. Hu, C. Battaglia, Y. Yang, *Nat. Commun.* **2021**, *12*, 5320; b) X. Ou, T. Liu, W. Zhong, X. Fan, X. Guo, X. Huang, L. Cao, J. Hu, B. Zhang, Y. S. Chu, G. Hu, Z. Lin, M. Dahbi, J. Alami, K. Amine, C. Yang, J. Lu, *Nat. Commun.* **2022**, *13*, 2319.
[23] G. Assat, C. Delacourt, D. A. Dalla Corte, J.-M. Tarascon, *J. Electrochem. Soc.* **2016**, *163*, A2965.

Manuscript received: May 8, 2023
Accepted manuscript online: October 6, 2023
Version of record online: October 23, 2023